Nuclear Engineering and Technology 51 (2019) 1406–1416

Contents lists available at ScienceDirect

Nuclear Engineering and Technology

journal homepage: www.elsevier.com/locate/net

Original Article

Multi-slit prompt-gamma camera for locating of distal dose falloff in proton therapy

Jong Hoon Park [a], Sung Hun Kim [a], Youngmo Ku [a], Chan Hyeong Kim [a, *], Han Rim Lee [b], Jong Hwi Jeong [c], Se Byeong Lee [c], Dong Ho Shin [d]

[a] Department of Nuclear Engineering, Hanyang University, 222, Wangsimni-ro, Seongdong-gu, Seoul, 04763, South Korea
[b] Neutron Utilization Technology Division, Korea Atomic Energy Research Institute, Daejeon, 34129, South Korea
[c] Proton Therapy Center, National Cancer Center, Goyang-si, Gyonggi-do 10408, South Korea
[d] IT Convergence Technology Research Laboratory, Electronics and Telecommunications Research Institute, Daejeon, 34129, South Korea

ARTICLE INFO

Article history:
Received 18 September 2018
Received in revised form
21 February 2019
Accepted 11 March 2019
Available online 13 March 2019

Keywords:
Proton therapy
Prompt gamma
Beam range verification
Distal dose falloff

ABSTRACT

In this research, a multi-slit prompt-gamma camera was developed to locate the distal dose falloff of the proton beam spots in spot scanning proton therapy. To see the performance of the developed camera, therapeutic proton beams were delivered to a solid plate phantom and then the prompt gammas from the phantom were measured using the camera. Our results show that the camera locates the 90% distal dose falloff (= d90%), within about 2–3 mm of error for the spots which are composed 3.8×10^8 protons or more. The measured location of d90% is not very sensitive to the irradiation depth of the proton beam (i.e., the depth of proton beam from the phantom surface toward which the camera is located). Considering the number of protons per spot for the most distal spots in typical treatment cases (i.e., 2 Gy dose divided in 2 fields), the camera can locate d90% only for a fraction of the spots depending on the treatment cases. However, the information of those spots is still valuable in that, in the multi-slit prompt-gamma camera, the distal dose falloff of the spots is located solely based on prompt gamma measurement, i.e., not referring to Monte Carlo simulation.

1. Introduction

Real-time locating of the distal dose falloff of proton beam spots in the patient is important in spot scanning proton therapy, not only for the safety of the patient but also for the effectiveness of treatment. Note that the main advantage of the proton beam over the conventional X-ray or electron beam is the finite range of the beam with a high gradient of dose at the end of the beam. However, this advantage is not fully utilized in current clinical practice for tight confirmation due to the uncertainty of the distal dose falloff location (= uncertainty of the beam range) in the patient, which is caused by the dose calculation error in the treatment planning system, patient positioning errors, inter- and intra-fractional anatomical changes, and so on. Therefore, in clinical practice, dose conformation through lateral dose shaping is mostly used, and this tangential avoidance of critical structures and use of patch fields increase the complexity of treatment and the number of the proton beams [1]. Real-time locating of the distal dose falloff of the proton beam spots would solve the problem and improve the effectiveness of treatment in the proton therapy.

The distal dose falloff in the patient cannot be located by measuring the protons simply because most protons completely stop in the patient. Therefore, two indirect methods have been proposed. One is to measure the 511-keV annihilation photons from the positron emitters produced by nuclear reactions along the proton beam passage in the patient with a positron emission tomography (PET) scanner [2]. However, the positron emitters have relatively long half-lives (i.e., 2–20 min) and, therefore, the PET imaging is not suitable for real-time monitoring. Moreover, there is a relatively poor correlation between the distributions of proton dose and positron emitters [3]. The method also suffers from the biological washout effect.

The other method is to measure the prompt gammas produced by nuclear reactions along the proton beam passage. Min et al. [4], for the first time, experimentally showed the correlation between the distributions of prompt gammas and proton dose. Unlike the positron emitters, the prompt gammas distribution has a very close

* Corresponding author.
E-mail address: chkim@hanyang.ac.kr (C.H. Kim).

https://doi.org/10.1016/j.net.2019.03.008

correlation with proton dose distribution at the end of the beam [3]. Currently, several research groups are developing different types of prompt-gamma measurement systems, such as the knife-edge slit camera [5–8], Compton camera [9–13], gamma electron vertex imaging (GEVI) system [14,15], and prompt gamma timing (PGT) system [16,17], to locate the distal dose falloff in real time during treatment.

The knife-edge slit camera is currently the most mature system with very high imaging efficiency, but the prompt-gamma distributions measured by the camera always show low gradient at the distal dose falloff. In addition, the measured prompt-gamma distribution significantly depends on the position of the beam spot; that is, the knife-edge slit camera shows a different distribution of prompt gammas even for an identical proton beam spot if the longitudinal or lateral position of the spot is different in the patient. For a proper measurement, therefore, the center of the knife-edge slit should be located near the expected location of the distal dose falloff, which is disadvantageous for large targets, requiring relocation of the camera. The field-of-view (FOV) or the imaging volume is also limited due to the structure of the knife-edge slit in the camera. The FOV can be increased by increasing the distance between the patient and the camera, which would result in reduction of measurement counting efficiency. Finally, it is known that the knife-edge slit camera cannot directly locate the distal dose falloff of the proton beam spots solely based on the measured distribution of prompt gammas; instead, the location of the distal dose falloff is predicted by comparing the measured prompt-gamma distribution from the knife-edge slit camera with the reference distribution either from Monte Carlo simulation or from another measurement [18].

We believe that a multi-slit prompt-gamma camera that consists of a multiple-parallel-slit collimation system and an array of detectors (Fig. 1) can overcome the limitations of the knife-edge slit camera. Our experience from preliminary studies [19] shows that the multi-slit prompt-gamma camera tends to provide high-gradient prompt-gamma distributions that abruptly decrease at the distal dose falloff. The measured distribution of prompt gammas of a multi-slit prompt-gamma camera also tends to be less sensitive to the longitudinal or lateral position of the proton beam spot in the patient, which makes easier to combine the prompt-gamma distributions of neighboring spots, as necessary, to improve the counting statistics. In addition, the FOV of the multi-slit prompt-gamma camera is not limited; that is, it can be increased simply by increasing the number of detectors. Most importantly, in contrast to the knife-edge slit camera, the multi-slit prompt-gamma camera can directly locate the distal dose falloff of the proton beam spots solely based on prompt gamma measurement, i.e., not referring to Monte Carlo simulation.

In the present study, we developed a new multi-slit prompt-gamma camera that is composed of two detector blocks and a dedicated dual-mode readout system for the detectors in the detector blocks. Then, the performance of the camera was evaluated by measuring the prompt gammas from a solid plate phantom to which therapeutic proton beams with different energies were delivered.

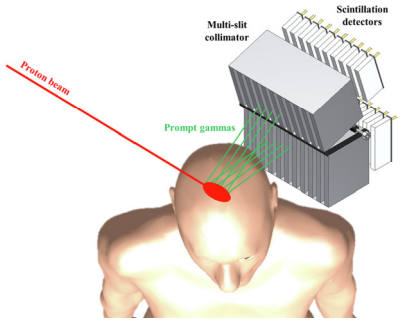

Fig. 1. Concept of multi-slit prompt-gamma camera.

2. Material and methods

2.1. Component of the multi-slit prompt-gamma camera

2.1.1. Multi-slit collimators

The multi-slit collimators, which is made of tungsten, are used to selectively detect the prompt gammas that are emitted perpendicular to the proton beam passage. The optimal thickness of the slit and the septal were determined to be 2 mm in the previous study [19] of Monte Carlo simulation, resulting in slit pitch of 4 mm. The height of the slit was set to 100 mm to match the size of the CsI(Tl) scintillation detector. The length of the slit was set to 100 mm to keep a septal penetration of the unwanted radiations below 10% [20]. To overcome the physical limitations of the 4 mm slit pitch, the two detector blocks were constructed and placed in a staggered arrangement, providing 2 mm slit pitch (Fig. 2). Note that the angle between the two detector blocks can be changed to focus the detector blocks at the treatment volume and maximize the counting efficiency.

2.1.2. Photo-sensor

To configure a scintillation detector for prompt-gamma measurement, we used photodiodes as photo-sensor. We did not use silicon photomultipliers (SiPMs) mainly because these are known to be very sensitive to neutron field [21,22], which might become a practical problem for prolonged usage of the camera in clinics. In addition, the SiPMs do not show a good linearity in energy calibration when the photon energy is very high. For example, there is a case where an exponential curve was used in energy calibration because the linearity was disrupted in the measurement of prompt gammas at energies higher than 3 MeV [7]. This is not a critical problem, but makes the energy calibration more difficult and uncertain because we are interested in the prompt gammas that have the energy range of 4–10 MeV. The photodiode, on the other hand, shows a very linear response in energy calibration even for high-energy gammas and relatively strong radiation hardness when compared to the SiPMs [23].

2.1.3. Scintillator

In the present study, we used the CsI(Tl) scintillator, which is inexpensive and the peak wavelength of 550 nm matches very well

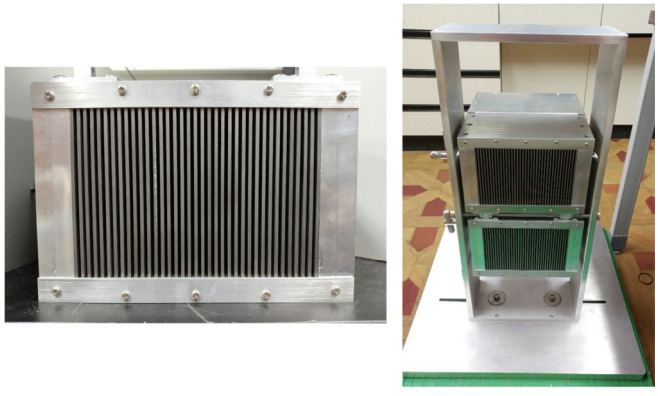

Fig. 2. Multi-slit collimator (left) and two detector blocks, each of which is composed of a multi-slit collimator and 36 CsI(Tl) scintillation detectors (right).

with the Si PIN photodiode. It also has a relatively high light yield (50,000–60,000 photons/MeV) compared to the other scintillators. Most importantly, the CsI(Tl) scintillator rarely responds to neutrons; that is, the neutrons rarely deposit energy greater than the threshold level (= 3 MeV) of the camera due to high atomic weights of the component elements (Cs: 132.9, I: 126.9, and Tl: 204.4 amu), which is a significant advantage over the other scintillators in prompt gamma measurement.

In the present study, thin CsI(Tl) scintillators (Hangzhou Lambda Photonics Technology Co., China) of 3 × 30 × 100 mm^3 were coupled to 3 × 30 mm^2 Si PIN photodiodes (S3588-08, Hamamatsu Photonics K.K., Japan), which show relatively fast response with a rise time (from 10% to 90%) of ~20 ns. The entire surfaces of each scintillator, except for the surface optically coupled to the photodiode, were treated with the Enhanced Specular Reflector (ESR; 3 M, MN), which has reflectivity higher than 98%. The scintillator and the photodiode were coupled with the silicon optical grease (BC-630, Saint-Gobain Crystals, France), showing 95% beam transmittance. Finally, the scintillator and the photodiode was wrapped with a Teflon tape to block the light from the environment.

2.1.4. Dual-mode readout system

In the present study, a dual-mode readout system was developed for total 72 scintillation detectors in the camera [24]. The developed system operates in two modes: the energy calibration mode and the fast data acquisition mode. In the energy calibration mode, the energy spectra are obtained for an automated energy calibration of the 72 detectors. In the fast data acquisition mode, the prompt gammas that deposit energy higher than 3 MeV in the detectors are simply counted, and the distribution of the prompt gammas over the detectors is displayed and analyzed in real time. Note that for the most cases, the high-energy prompt gammas are not fully absorbed in the detector. This is because pair production is the dominant process and the two 511-keV annihilation photons mostly escape the thin scintillation detector. To measure the prompt gammas including the double-escape peak (= 3.42 MeV) of the 4.44 MeV prompt gammas based on interactions of ^{16}O (p,x)^{12}C, ^{12}C (p,p')^{12}C, and ^{12}C (p,x)^{11}B which are most abundant, the threshold level for prompt gamma measurement was set to 3 MeV. Fig. 3 shows the circuit schematic diagram of the dual-mode readout system.

The steps for processing the signals from the 72 scintillation detectors are as follows. First, the signal from each detector goes through an AC coupling and then pre-amplified in a CR-110 chip (Cremat Inc., MA), a charge sensitive preamplifier. Then, the output signal of the preamplifier is split in two and shaped into a Gaussian-like shape by a shaper [15] with different shaping times: 4 μs for energy measurement and 500 ns for triggering. After shaping, the signals are processed by an energy calibration system or a fast data acquisition system depending on the measurement situation.

In the system for energy calibration, a total of six multiplexing systems [25] are used to reduce the 72 channels of the detector signals to 12 channels containing the identification number of the detector interacted by the prompt gamma and the amount of the energy deposited in the detector. In a multiplexing system, a comparator generates a trigger signal (TTL/CMOS logic-compatible signal) if the detector signal exceeds a threshold level. The trigger signal is fed into the primary encoder and it produces the identification number of the detector where the signal was generated. The multiplexer (ADG1606, Analog Devices Inc., MA) receives the signal of the identification number of the detector and passes only the energy signal generated from the detector. During the process, a single-pole-single-through (SPST) switch and a monostable multivibrator block subsequent trigger signals. The signals passed by the multiplexer are then simultaneously acquired by a digitizer (PXI-5105, National Instrument, TX). Based on the acquired information, the energy spectrum is produced for each detector and the 72 detectors are energy-calibrated in an automated process.

In the system for fast data acquisition, for each detector, the amplitude of the detector signal is compared with the predefined threshold level, corresponding to 3 MeV, in the comparator (AD8564, Analog Devices Inc., MA) and a logic signal is generated if the signal is greater than the predefined level. The microcontroller (Arduino Due, Arduino, Italy) counts the logic signals from each

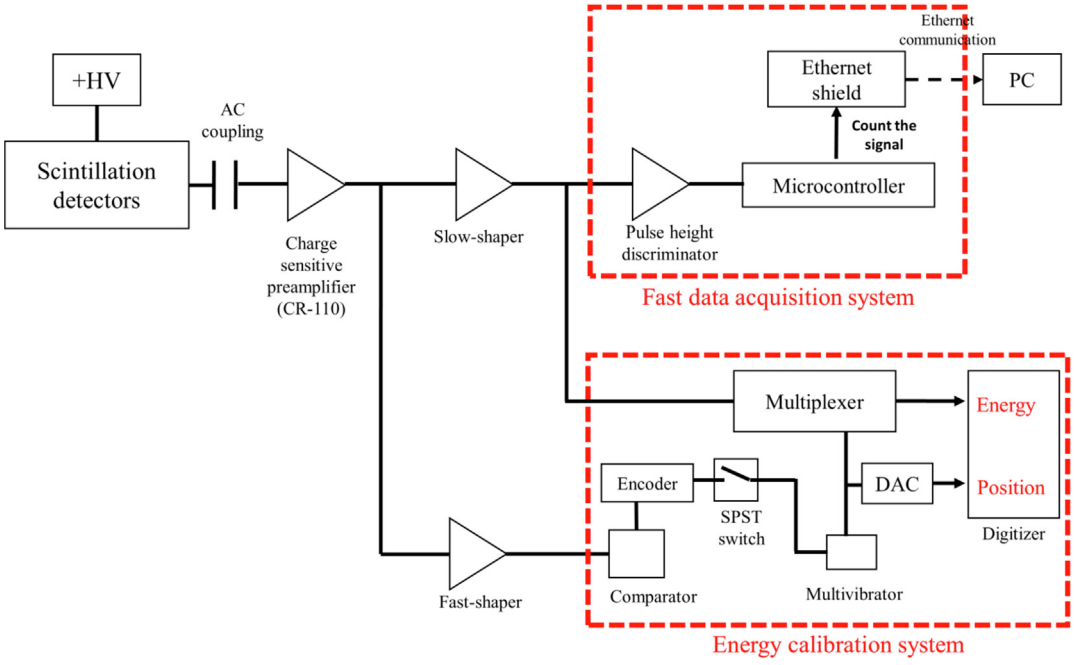

Fig. 3. Schematic diagram of the dual-mode readout system.

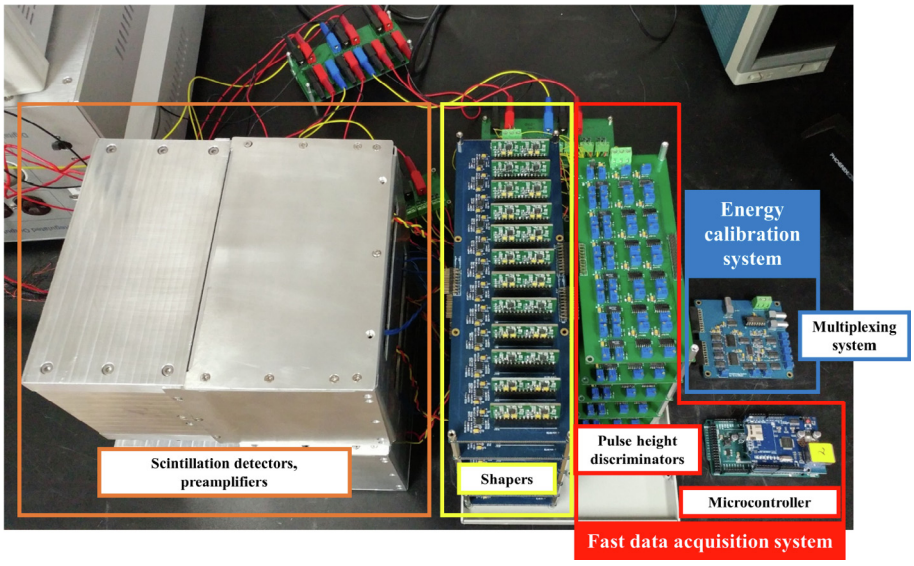

Fig. 4. Multi-slit prompt-gamma camera composed of CsI(Tl) scintillation detectors, preamplifiers, shapers, pulse height discriminators, multiplexing systems, and microcontrollers. The digitizer used in the energy calibration system is not shown in the picture.

detector and sends the information to a PC via an Ethernet communication (Arduino Ethernet W5100 Shield, WIZnet, Republic of Korea). Finally, the number of counts from the 72 detectors produces a one-dimensional distribution of prompt gammas in the beam direction.

The Arduino Due microcontroller (clock speed: 84 MHz), which was used for fast counting, can process 27,000 signals per second in each channel when the signals are given to the 12 input channels at the same time. If only one channel is used for input, it can process up to 136,000 signals per second. This shows that the microcontroller can process the signals from a proton beam current of 2–5 nA, which is usually used in proton therapy. Even if we conservatively assume that the probability of having a signal of prompt gamma greater than 3 MeV in a detector is 8×10^{-7} per incident proton, the microcontroller can process all of the signals.

Fig. 4 shows the developed multi-slit prompt-gamma camera, which is composed of two detector modules and a dual-mode readout system for the detectors. The aluminum case was used to shield the scintillation detectors and preamplifiers from the light and electromagnetic disturbances from outside.

2.2. Evaluation of the performance of the multi-slit prompt-gamma camera

2.2.1. Energy calibration for gamma-ray sources

The energy calibration of the 72 scintillation detectors was performed using the gamma-ray sources of ^{22}Na (511 keV, 1275 keV, activity: 3.47 μCi) and ^{137}Cs (662 keV, activity: 8.22 μCi). The sources were located at 20 cm from the multi-slit prompt-gamma camera, and for each source, the energy spectra were measured by the 72 detectors of the camera for 2 h. For this measurement, the multi-slit collimators were removed from the

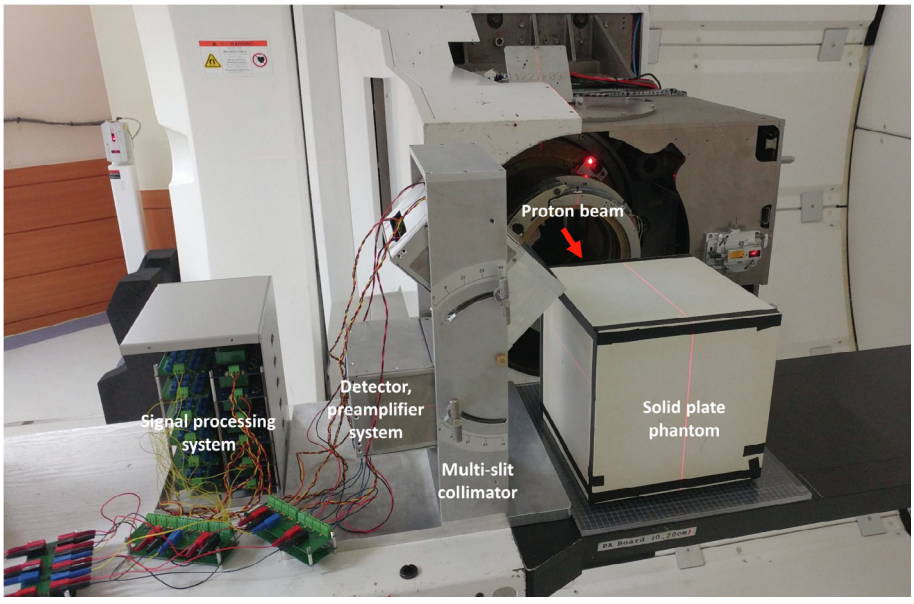

Fig. 5. Experimental setup for prompt gamma measurement using multi-slit prompt-gamma camera.

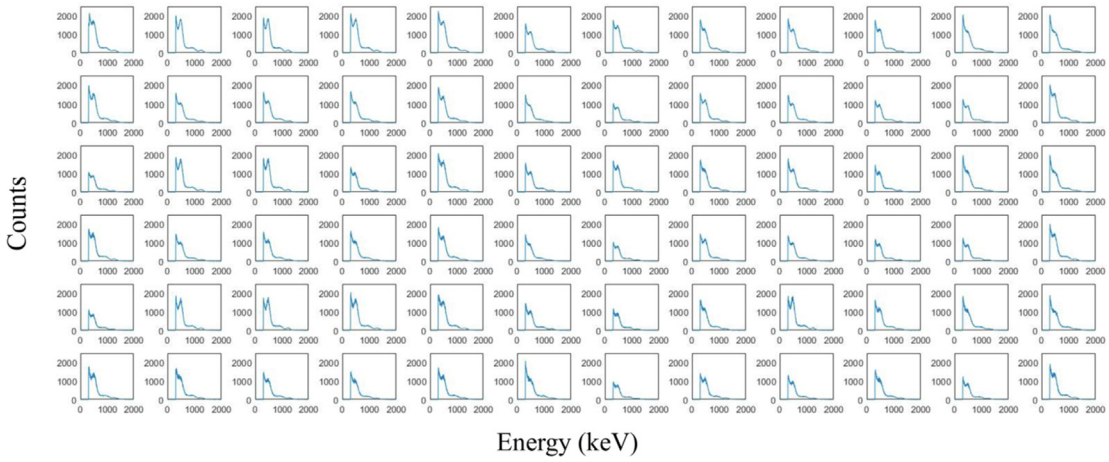

Fig. 6. Energy spectra of ^{22}Na source measured by 72 detectors in multi-slit prompt-gamma camera.

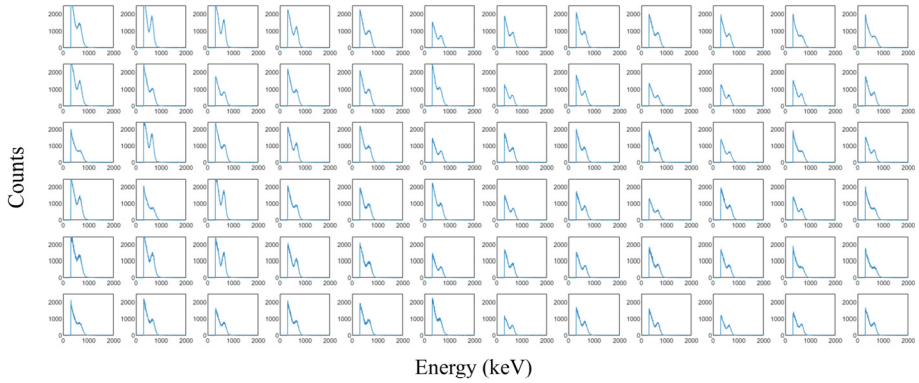

Fig. 7. Energy spectra of ^{137}Cs source measured by 72 detectors in multi-slit prompt-gamma camera.

camera. Based on the measured spectra obtained for the 72 detectors, each of the detectors is energy-calibrated in an automated process with an in-house computer program written in MATLAB, which automatically identifies the full-energy peaks in the energy spectra and also calculates the energy resolution for each peak.

Based on the result of the energy calibration, for each detector, the threshold level corresponding to 3 MeV energy deposition was determined and applied to the pulse height discriminator (= comparator) of the fast data acquisition system.

2.2.2. *Performance evaluation for therapeutic proton beam*

The performance of the multi-slit prompt-gamma camera was evaluated using the therapeutic proton beams of the proton therapy machine (Proteus 235, IBA, Belgium) at the National Cancer Center in Korea. Fig. 5 shows the experimental setup to measure the prompt-gamma distribution with the camera. The solid plate phantom (SP34, composition: 98% polystyrene + 2% TiO_2, IBA, Germany) of $30 \times 30 \times 30$ cm^3 was located on the treatment couch, and the camera was positioned at 10 cm from the phantom surface. The angle between the two detector blocks was set to 45°. The proton pencil beam from a scanning nozzle was delivered at a depth of 10 cm from the phantom surface where the camera was located. The used beam energies were 95.09, 122.6, 146.45, and 186.3 MeV. To reduce the effect of the neutrons and background gammas, a 5-cm-thick shield of lead bricks was installed between the beam nozzle and the camera.

To evaluate the performance of the developed camera, the prompt-gamma distributions in the solid plate phantom were measured with the camera changing the number of delivered protons and proton beam energies. Then, prompt-gamma distributions were also measured changing the irradiation depth, which is the depth of proton beam from the phantom surface toward which the camera is located, to see if the measured location of the distal dose falloff significantly changes as we change the depth of irradiation.

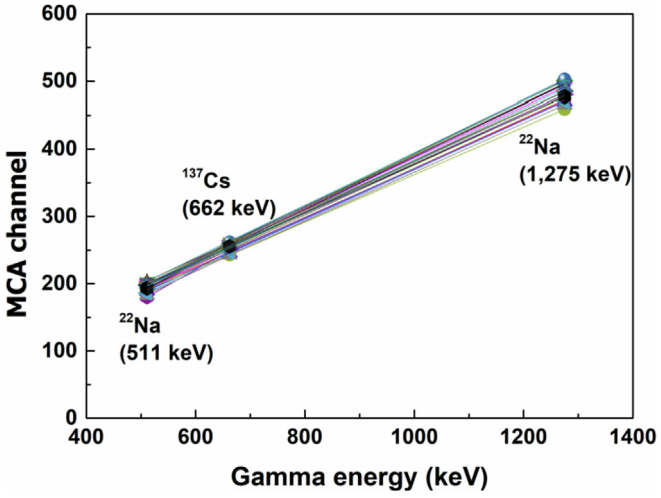

Fig. 8. Energy calibration curve of 72 detectors in multi-slit prompt-gamma camera.

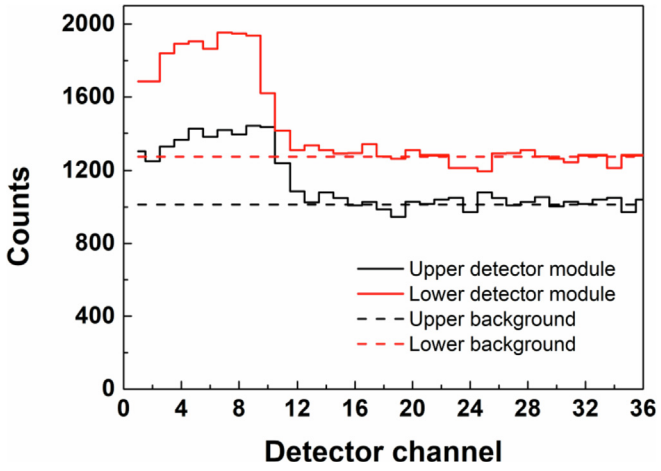

Fig. 9. Prompt-gamma distributions (solid lines) measured with two detector modules in multi-slit prompt-gamma camera for 95.09 MeV proton beam, with background levels (broken lines).

3. Results and discussions

3.1. Energy calibration for gamma-ray sources

Figs. 6 and 7 show the energy spectra of the ^{22}Na (511 keV, 1275 keV) and ^{137}Cs (662 keV) sources measured by the 72 detectors in the developed camera. For all of the detectors, the full-energy peaks of the sources were successfully identified. The average energy resolutions of the detectors were 25.8% ± 2.4%p, 22.1% ± 1.8%p, and 12.1% ± 0.9%p for 511, 662, and 1275 keV gamma-ray peaks, respectively.

The full-energy peaks of the gamma-ray sources were linearly regressed for energy calibration and the coefficient of determination (R^2) of the regression was 0.99 on the average (Fig. 8). The voltage value for the threshold level (= 3 MeV) was calculated using the linear regression equation for each detector. Note that, in a previous study [26], it was experimentally shown that this approach determines the 3 MeV of the threshold level within 3% of error. The voltage values were applied to the 72 comparators of the fast data acquisition system via variable registers.

3.2. Performance evaluation for therapeutic proton beam

Fig. 9 shows, as an example, the prompt-gamma distributions measured by the upper detector module (black solid line) and the lower detector module (red solid line) of the developed camera for the 95.09 MeV proton beam. The number of protons to obtain the distribution was 7.5 × 10^9 protons. Note that the upper and lower detector modules, which have 4 mm detection pitch, are placed in a staggered arrangement to provide 2 mm detection pitch.

To combine the prompt-gamma distributions of the two detector modules, the following procedure was used. First, the background level (broken line), which is the average value of prompt gamma counts of the detectors located beyond the distal dose falloff, is subtracted from each of the prompt-gamma distributions; then, the resulting distribution is normalized to the area of the distribution. Finally, the two normalized distributions were

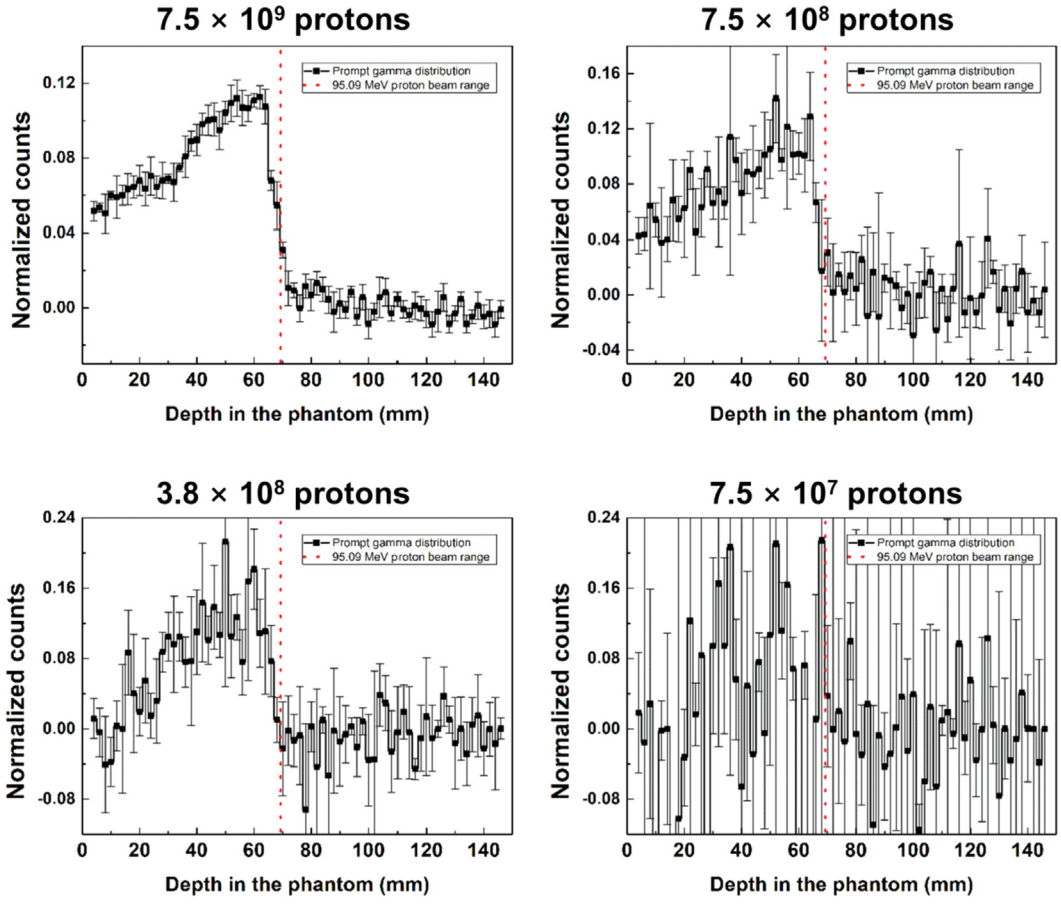

Fig. 10. Prompt-gamma distributions measured with the multi-slit prompt-gamma camera for different numbers of protons for the 95.09 MeV proton beam.

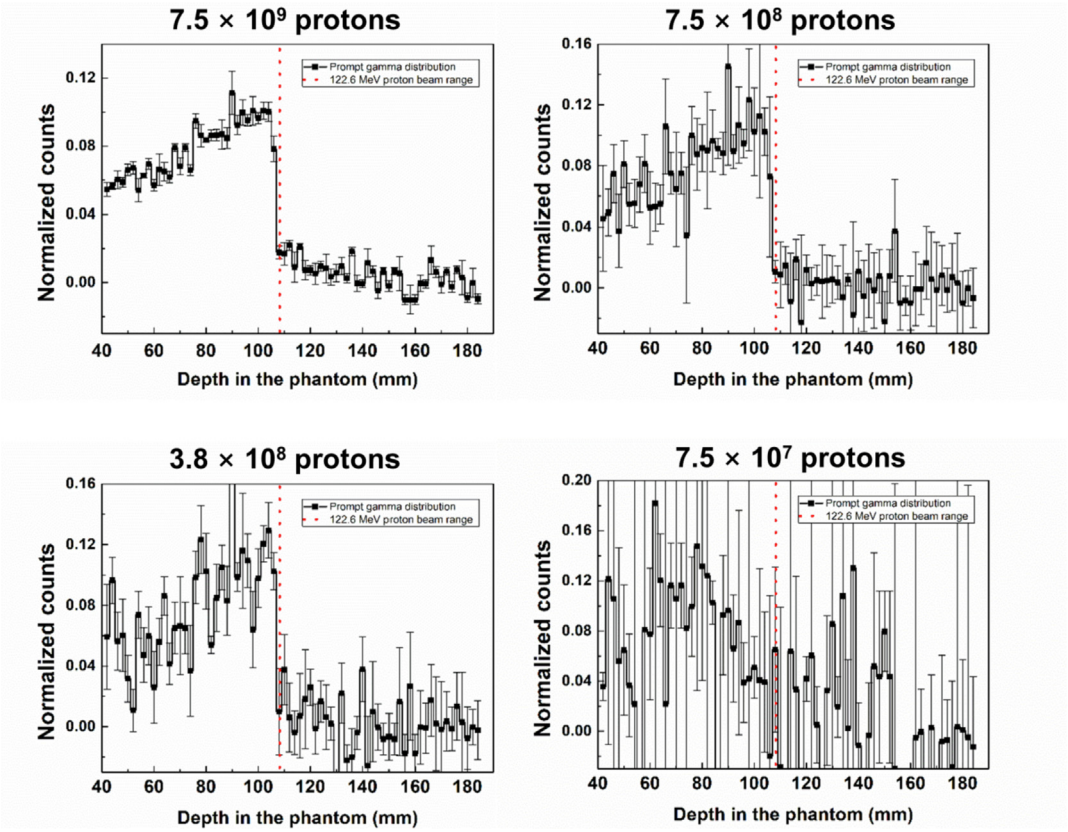

Fig. 11. Prompt-gamma distributions measured with the multi-slit prompt-gamma camera for different numbers of protons for the 122.6 MeV proton beam.

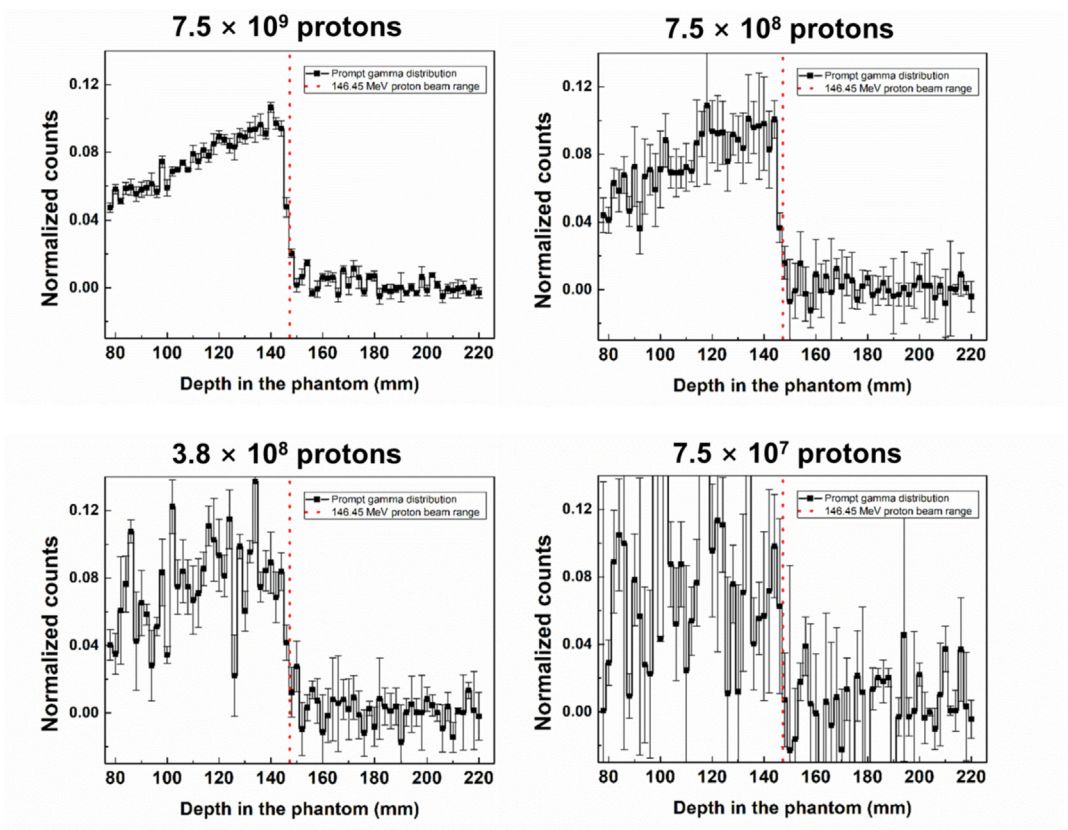

Fig. 12. Prompt-gamma distributions measured with the multi-slit prompt-gamma camera for different numbers of protons for the 146.45 MeV proton beam.

superimposed on a single plot with 2 mm shift for one detector to reflect the staggered arrangement of the detector blocks.

Figs. 10–13 show the prompt-gamma distributions measured with the multi-slit prompt-gamma camera for 95.09, 122.6, 146.45, and 186.3 MeV proton beams, respectively. The red vertical dotted lines in the plots show the locations of the 90% distal dose falloff (= d90%) measured by Gafchromic EBT3 film (ISP, NJ), which are 69.3, 108.2, 147.3, and 223.7 mm for 95.09, 122.6, 146.45, and 186.3 MeV proton beams, respectively. Note that, in the present study, the d90% is defined as the location of distal 90% dose in a depth-dose curve, and that the distance from the surface to the d90% corresponds to the range of the proton beam in a given medium. For each proton beam energy, the number of delivered protons were varied from 7.5×10^9 down to 7.5×10^7. For each case, the measurement was repeated 5 times to determine the statistical uncertainty of the measurement. The error bars in the plots indicate the statistical uncertainty (= one standard deviation) of the measured counts. It can be seen that the fluctuation in the distribution increases with the decrease of the number of delivered protons, as expected, meaning that the uncertainty in the measured d90% location increases with the decrease of the number of delivered protons. It can also be seen that, for all proton beam energies, the camera provides a very high gradient of prompt-gamma distribution at the d90%. The counting efficiency of the camera, which is the total number of counts from the 72 detectors in the camera divided by the number of the delivered proton, was 1.4×10^{-5}, 2.2×10^{-5}, 2.6×10^{-5}, and

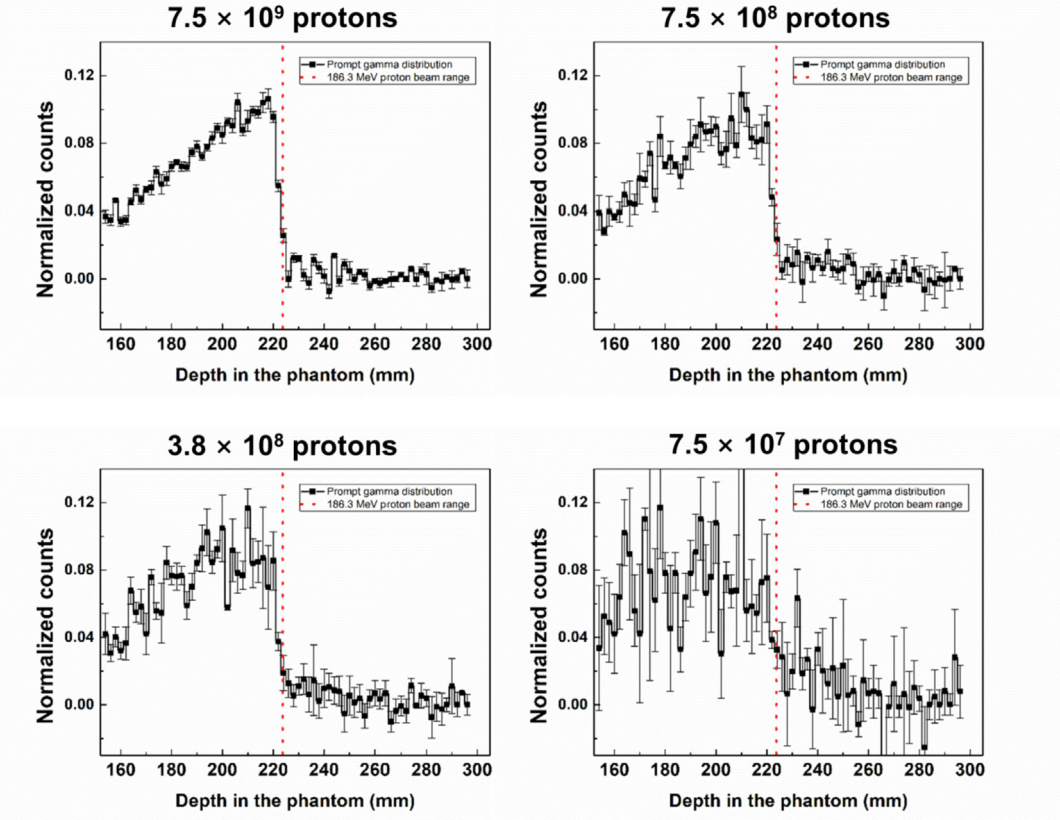

Fig. 13. Prompt-gamma distributions measured with the multi-slit prompt-gamma camera for different numbers of protons for the 186.3 MeV proton beam.

Table 1
Distal dose falloff location and uncertainty for the different number of delivered protons.

Beam energy (MeV)	Number of delivered protons	Measured 90% distal dose falloff	Error (mm)
95.09	7.5×10^7	–	–
	3.8×10^8	67.2 (1.2)	−2.1
	7.5×10^8	67.0 (0.9)	−2.3
	7.5×10^9	67.5 (0.2)	−1.8
122.6	7.5×10^7	–	–
	3.8×10^8	105.8 (1.0)	−2.4
	7.5×10^8	106.3 (0.7)	−1.9
	7.5×10^9	106.6 (0.1)	−1.6
146.45	7.5×10^7	–	–
	3.8×10^8	145.8 (0.4)	−1.5
	7.5×10^8	145.9 (0.5)	−1.4
	7.5×10^9	145.8 (0.2)	−1.5
186.3	7.5×10^7	–	–
	3.8×10^8	222.0 (0.4)	−1.7
	7.5×10^8	222.4 (0.4)	−1.3
	7.5×10^9	222.1 (0.2)	−1.6

3.3×10^{-5} counts/proton for 95.09, 122.6, 146.45, and 186.3 MeV proton beams, respectively.

On the measured prompt-gamma distribution, the d90% was located with sigmoidal curve fitting [19]. According to our investigation, when the number of delivered protons is equal to or greater than 3.8×10^8, the d90% was always correctly located by the camera. When the number of delivered protons was 7.5×10^7, however, the d90% was correctly located only for about 40% probability, which is due to large statistical fluctuations in the measured prompt-gamma distributions.

Table 1 shows the location of the d90% measured by the multi-slit prompt-gamma camera and the error from the actual location of the d90% which was measured with EBT3 film, for different proton energies and different numbers of delivered protons. The results show that the uncertainty is generally less than 1 mm, and that the error from the actual locations of the d90% measured by EBT3 film is less than 2–3 mm. Note that, in the present study, we simply take the inflection point of the sigmoidal curve as the

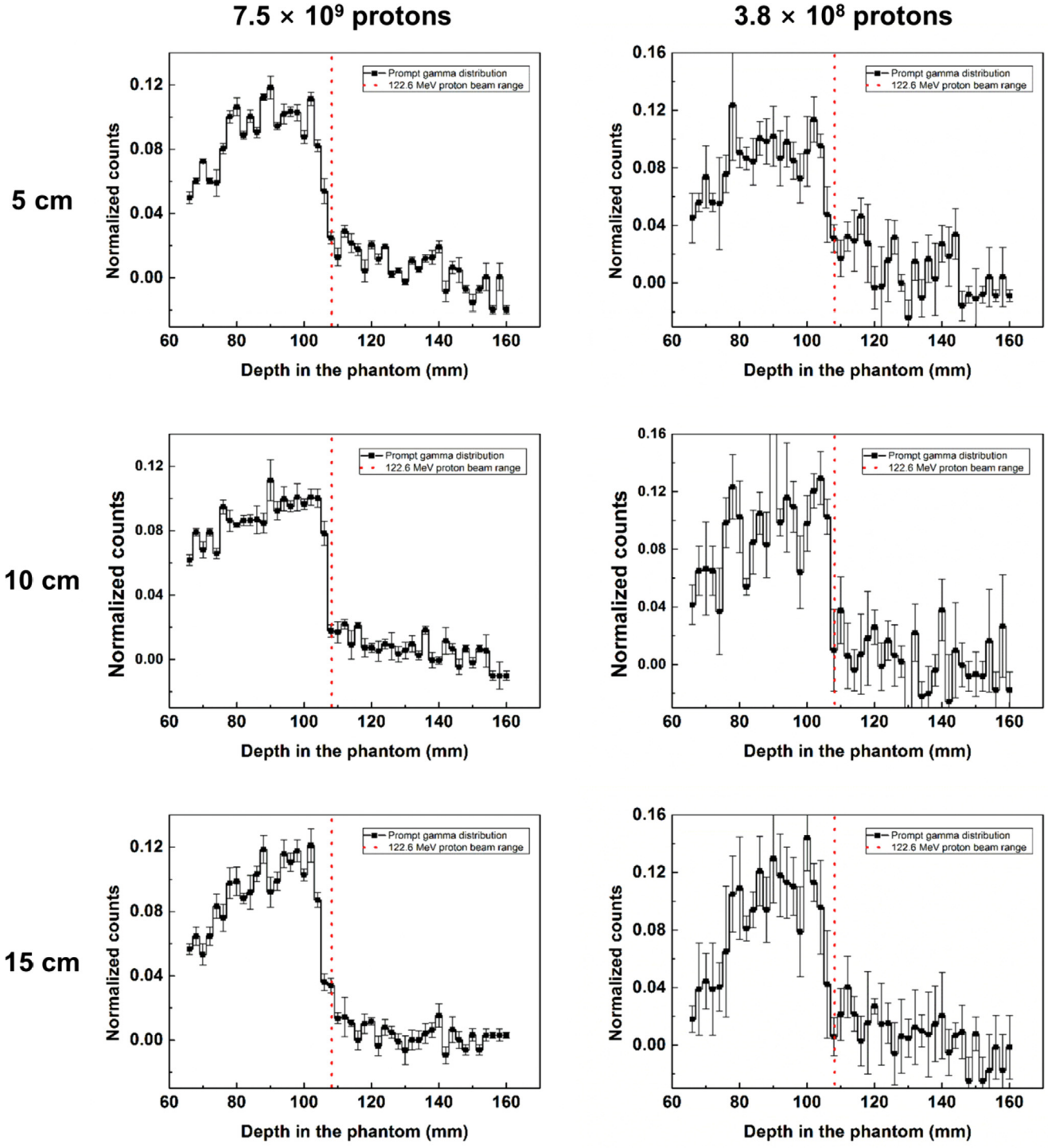

Fig. 14. Prompt-gamma distribution measured with the multi-slit prompt-gamma camera for different irradiation depths (5, 10, and 15 cm). The proton energy is 122.6 MeV.

location of the d90%, and we believe the measurement accuracy of the d90% can be improved in the future by carefully selecting a point in the sigmoidal curve as the distal falloff location.

Fig. 14 shows the prompt-gamma distributions measured by the multi-slit prompt-gamma camera for different irradiation depths (5, 10, and 15 cm). The number of protons to obtain the distribution was 7.5×10^9 and 3.8×10^8 protons. The red vertical dotted lines show the location of the range (= 108.2 mm) of the 122.6 MeV proton beam in the phantom, which was measured by EBT3 film. For 7.5×10^9 protons, the estimated d90% locations were 106.1($1\sigma = 0.1$), 106.3(0.1), and 106.9 (0.2) mm for irradiation depths of 5, 10, and 15 cm, respectively. For 3.8×10^8 protons, the estimated d90% locations were 106.4(1.1), 105.8(1.0), and 107.2 (1.2) mm for irradiation depths of 5, 10, and 15 cm, respectively. The counting efficiency of the camera decreased from 3.0×10^{-5} to 1.6×10^{-5} counts/proton as the irradiation depth increases from 5 to 15 cm. Nevertheless, the results show that the measured location of the d90% barely changes as we change the irradiation depth of the proton beam in the phantom.

Considering that the number of protons per spot ranges approximately from 10^7 to 10^9 for the most distal spots for a typical 2 Gy treatment with 2 fields, the camera can locate the d90% only for a fraction of the spots depending on the cases. However, the information of those spots is still valuable in that, in the multi-slit prompt-gamma camera, the d90% of the spots is located solely based on prompt gamma measurement, i.e., not referring to Monte Carlo simulation.

Note that the number of protons per spot will be increased by factor of a few times as we use hypo-fractionation, instead of the conventional 2 Gy treatment, in which case we can locate the d90% for more spots using the camera. In addition, the statistics of measurement could be further improved by merging the prompt-gamma distributions of neighboring spots. The summed prompt-gamma distribution of the entire spots in each layer of the proton beam spots would also provide very sensitive indication of the inter-fractional changes of patient anatomy and positioning.

4. Conclusion

In the present study, we developed a multi-slit prompt-gamma camera to locate the distal dose falloff of the proton beam spots. The developed camera is made of two detector blocks, each of which is composed of a multi-slit collimator and 36 CsI(Tl) scintillation detectors, and a dedicated dual-mode readout system for the detectors in the detector blocks. To evaluate the performance of the camera, therapeutic proton beams were delivered to a solid plate phantom and then the prompt gammas from the phantom were measured using the camera. Our results show that the camera locates the distal dose falloff (= d90%), which is defined as the depth of distal 90% dose in a depth-dose curve, within about 2–3 mm of error for the spots which are composed of 3.8×10^8 protons or more. It was also found that the location of d90% is not very sensitive to the irradiation depth of the proton beam in the phantom. Considering the number of protons per spot, the camera can locate d90% only for a fraction of the spots, depending on the cases, in typical treatment cases (2 Gy dose divided in 2 fields), which is still valuable in that, in the multi-slit prompt-gamma camera, the d90% of the spots is located solely based on prompt gamma measurement, i.e., not referring to Monte Carlo simulation. Note that the detection efficiency of the camera could be increased by a few times, as necessary in the future, by further optimizing the camera, e.g., (1) by using more detector modules, (2) by increasing the size of the scintillator, which would require custom-made photodiodes to match the dimensions, and (3) by decreasing the length of the slit of the multi-slit collimator.

Acknowledgments

This work was partly supported by Electronics and Telecommunications Research Institute (ETRI) R&D Program (Development of particle beam range verification technology based on prompt gamma-ray measurements, 15ZC1810) and by the Nuclear Safety Research and Development (NSR&D) Program through the Korea Foundation of Nuclear Safety (KoFONS) funded by the Nuclear Safety and Security Commission (NSSC) (Project Number: 1705006).

References

[1] T.F. DeLaney, H.M. Kooy, Proton and Charged Particle Radiotherapy, Lippincott Williams & Wilkins, 2008.
[2] U. Oelfke, G.K.Y. Lam, M.S. Atkins, Proton dose monitoring with PET: quantitative studies in Lucite, Phys. Med. Biol. 41 (1996) 177–196.
[3] M. Moteabbed, S. Espana, H. Paganetti, Monte Carlo patient study on the comparison of prompt gamma and PET imaging for range verification in proton therapy, Phys. Med. Biol. 56 (2011) 1063–1082.
[4] C.H. Min, C.H. Kim, M.Y. Youn, J.W. Kim, Prompt gamma measurements for locating the dose falloff region in the proton therapy, Appl. Phys. Lett. 89 (2006).
[5] J. Smeets, F. Roellinghoff, D. Prieels, F. Stichelbaut, A. Benilov, P. Busca, C. Fiorini, R. Peloso, M. Basilavecchia, T. Frizzi, J.C. Dehaes, A. Dubus, Prompt gamma imaging with a slit camera for real-time range control in proton therapy, Phys. Med. Biol. 57 (2012) 3371–3405.
[6] V. Bom, L. Joulaeizadeh, F. Beekman, Real-time prompt gamma monitoring in spot-scanning proton therapy using imaging through a knife-edge-shaped slit, Phys. Med. Biol. 57 (2012) 297–308.
[7] I. Perali, A. Celani, L. Bombelli, C. Fiorini, F. Camera, E. Clementel, S. Henrotin, G. Janssens, D. Prieels, F. Roellinghoff, J. Smeets, F. Stichelbaut, F.V. Stappen, Prompt gamma imaging of proton pencil beams at clinical dose rate, Phys. Med. Biol. 59 (2014) 5849–5871.
[8] M. Priegnitz, S. Helmbrecht, G. Janssens, I. Perali, J. Smeets, F. Vander Stappen, E. Sterpin, F. Fiedler, Detection of mixed-range proton pencil beams with a prompt gamma slit camera, Phys. Med. Biol. 61 (2016) 855–871.
[9] M. Frandes, A. Zoglauer, V. Maxim, R. Prost, A tracking compton-scattering imaging system for hadron therapy monitoring, IEEE Trans. Nucl. Sci. 57 (2010) 144–150.
[10] M.H. Richard, M. Chevallier, D. Dauvergne, N. Freud, P. Henriquet, F. Le Foulher, J.M. Létang, G. Montarou, C. Ray, F. Roellinghoff, E. Testa, M. Testa, A.H. Walenta, Design guidelines for a double scattering compton camera for prompt-γ Imaging during ion beam therapy: a Monte Carlo simulation study, IEEE Trans. Nucl. Sci. 58 (2011) 87–94.
[11] D. Mackin, S. Peterson, S. Beddar, J. Polf, Evaluation of a stochastic reconstruction algorithm for use in Compton camera imaging and beam range verification from secondary gamma emission during proton therapy, Phys. Med. Biol. 57 (2012) 3537–3553.
[12] J. Krimmer, J.L. Ley, C. Abellan, J.P. Cachemiche, L. Caponetto, X. Chen, M. Dahoumane, D. Dauyergne, N. Freud, B. Joly, D. Lambert, L. Lestand, J.M. Letang, M. Magne, H. Mathez, V. Maxim, G. Montarou, C. Morel, M. Pinto, C. Ray, V. Reithinger, E. Testa, Y. Zoccarato, Development of a Compton camera for medical applications based on silicon strip and scintillation detectors, Nucl. Instrum. Methods Phys. Res. Sect. A Accel. Spectrom. Detect. Assoc. Equip. 787 (2015) 98–101.
[13] J.C. Polf, S. Avery, D.S. Mackin, S. Beddar, Imaging of prompt gamma rays emitted during delivery of clinical proton beams with a Compton camera: feasibility studies for range verification, Phys. Med. Biol. 60 (2015) 7085–7099.
[14] C.H. Kim, J.H. Park, H. Seo, H.R. Lee, Gamma electron vertex imaging and application to beam range verification in proton therapy, Med. Phys. 39 (2012) 1001–1005.
[15] H.R. Lee, J.H. Park, J.H. Kim, W.G. Jung, C.H. Kim, Development of signal processing modules for double-sided silicon strip detector of gamma vertex imaging for proton beam dose verification, J. Radiat. Prot. 39 (2014) 81–88.
[16] C. Golnik, F. Hueso-Gonzalez, A. Muller, P. Dendooven, W. Enghardt, F. Fiedler, T. Kormoll, K. Roemer, J. Petzoldt, A. Wagner, G. Pausch, Range assessment in particle therapy based on prompt gamma-ray timing measurements, Phys. Med. Biol. 59 (2014) 5399–5422.
[17] F. Hueso-González, W. Enghardt, F. Fiedler, C. Golnik, G. Janssens, J. Petzoldt, D. Prieels, M. Priegnitz, K.E. Römer, J. Smeets, F. Vander Stappen, A. Wagner, G. Pausch, First test of the prompt gamma ray timing method with heterogeneous targets at a clinical proton therapy facility, Phys. Med. Biol. 60 (2015) 6247–6272.
[18] M. Priegnitz, S. Helmbrecht, G. Janssens, I. Perali, J. Smeets, F. Vander Stappen, E. Sterpin, F. Fiedler, Measurement of prompt gamma profiles in inhomogeneous targets with a knife-edge slit camera during proton irradiation, Phys. Med. Biol. 60 (2015) 4849–4871.
[19] C.H. Min, H.R. Lee, C.H. Kim, S.B. Lee, Development of array-type prompt gamma measurement system for in vivo range verification in proton therapy,

Med. Phys. 39 (2012) 2100–2107.
[20] S.R. Cheery, J.A. Sorenson, M.E. Phelps, Physics in Nuclear Medicine, Elsevier, PA: Saunders, 2013.
[21] M. Andreotti, W. Baldini, R. Calabrese, G. Cibinetto, A.C. Ramusino, C. De Donato, R. Faccini, M. Fiorini, E. Luppi, R. Malaguti, A. Montanari, A. Pietropaolo, V. Santoro, G. Tellarini, L. Tomassetti, N. Tosi, Study of the radiation damage of Silicon Photo-Multipliers at the GELINA facility, J. Instrum. 9 (2014).
[22] R. Pagano, S. Lombardo, F. Palumbo, D. Sanfilippo, G. Valvo, G. Fallica, S. Libertino, Radiation hardness of silicon photomultipliers under ^{60}Co γ-ray irradiation, Nucl. Instrum. Methods Phys. Res. Sect. A Accel. Spectrom. Detect. Assoc. Equip. 767 (2014) 347–352.
[23] D.G. Charlton, J.D. Dowell, R.J. Homer, P. Jovanovic, I.R. Kenyon, G. Mahout, H.R. Shaylor, A. Sibley, J.A. Wilson, J.H. Bibby, I.M. Gregor, R.L. Wastie, A.R. Weidberg, Radiation hardness and lifetime studies of photodiodes for the optical readout of the ATLAS semiconductor tracker, Nucl. Instrum. Methods Phys. Res. Sect. A Accel. Spectrom. Detect. Assoc. Equip. 456 (2001) 300–309.
[24] J.H. Park, H.R. Lee, S.H. Kim, C.H. Kim, D.H. Shin, S.B. Lee, J.H. Jeong, Development of dual-mode signal processing module for multi-slit prompt-gamma camera, Kor. J. Med. Phys. 27 (2016) 37–45.
[25] H.R. Lee, J.H. Park, H.S. Kim, C.H. Kim, Development of multiplexing system for reduction of data acquisition channels of multi-channel radiation, in: The Korean Association for Radiation Protection Spring Meeting, Korea, April 24-26, 2013.
[26] H.R. Lee, J.H. Park, S.H. Kim, C.H. Kim, Development of prompt gamma measurement system based on CsI(Tl) detector array for proton beam range verification, in: IEEE Nuclear Science Symposium and Medical Imaging Conference and 19th International Workshop on Room-Temperature Semiconductor X-Ray and Gamma-Ray Detectors, USA, October 27 – November 3, 2012.